Discretizations in isogeometric analysis of Navier-Stokes flow

Nørtoft, Peter; Gersborg, Allan Roulund; Gravesen, Jens; Pedersen, Niels Leergaard

Published in:
Computer Methods in Applied Mechanics and Engineering

Link to article, DOI:
10.1016/j.cma.2011.06.007

Publication date:
2011

Document Version
Peer reviewed version

Discretizations in Isogeometric Analysis of Navier-Stokes Flow

Peter Nørtoft Nielsen[a,b,*], Allan Roulund Gersborg[b,1], Jens Gravesen[a], Niels Leergaard Pedersen[b]

[a]*DTU Mathematics, Technical University of Denmark, Matematiktorvet 303S, DK-2800 Kgs. Lyngby, Denmark*
[b]*DTU Mechanical Engineering, Technical University of Denmark, Nils Koppels All 404, DK-2800 Kgs. Lyngby, Denmark*

Abstract

This paper deals with isogeometric analysis of the 2-dimensional, steady state, incompressible Navier-Stokes equation subjected to Dirichlet boundary conditions. We present a detailed description of the numerical method used to solve the boundary value problem. Numerical inf-sup stability tests for the simplified Stokes problem confirm the existence of many stable discretizations of the velocity and pressure spaces, and in particular show that stability may be achieved by means of knot refinement of the velocity space. Error convergence studies for the full Navier-Stokes problem show optimal convergence rates for this type of discretizations. Finally, a comparison of the results of the method to data from the literature for the the lid-driven square cavity for Reynolds numbers up to 10,000 serves as benchmarking of the discretizations and confirms the robustness of the method.

Keywords:
isogeometric analysis, fluid mechanics, Navier-Stokes flow, inf-sup stability, lid-driven square cavity

1. Introduction

Isogeometric analysis unites the power to solve complex engineering problems from finite element analysis (FEA) with the ability to smoothly represent complicated shapes in very few degrees of freedom from computer aided design (CAD) [1, 2]. Within recent years, isogeometric analysis has been applied to various flow problems and proved its value within the field of fluid mechanics. Some of the first studies were on steady-state incompressible Stokes flow in the benchmarking lid-driven square cavity [3]. Subsequent analysis of the full time dependent Navier-Stokes equations using the isogeometric method has shown its advantages both in terms of continuity of state variables [4] and the ability to accurately represent complicated dynamic flow domains [5]. Benchmarking of the method for the turbulent Taylor-Couette flow shows very nice performance of the method [6].

An important issue in the analysis of the mixed formulation of the governing equations for fluids is the stability of the element, or discretization, used to approximate the state variables. The first stable B-spline discretization for the Stokes problem was proposed in [3]. Recently, two more families of stable B-spline discretizations were identified in [7], thereby further emphasizing how easily high degrees of continuity may be achieved in isogeometric analysis. Mathematical proofs of the stability of a range of discretizations have very recently been made [8, 9].

The aim of this paper is threefold. Firstly, we wish to extend the list of stable B-spline discretizations for the 2D steady state, incompressible Stokes problem. Secondly, we wish apply the method to the non-linear 2D steady state, incompressible Navier-Stokes problem and examine how these discretizations perform in terms of error convergence based on a flow problem with an analytical solution. Finally, the benchmarking lid-driven square cavity will be analysed and the results of the discretizations compared to data from the literature.

The outline of the paper is as follows. Section 2 presents the equations that govern problems in fluid mechanics, and section 3 outlines how the problem is solved using isogeometric analysis. In section 4 we perform a numerically test of different isogeometric discretizations in terms of stability, and an error convergence study for these discretizations is presented in section 5. Finally in section 6, a comparison of the dis-

*Corresponding author.
Email addresses: p.n.nielsen@mat.dtu.dk (Peter Nørtoft Nielsen), agersborg.hansen@gmail.com (Allan Roulund Gersborg), j.gravesen@mat.dtu.dk (Jens Gravesen), nlp@mek.dtu.dk (Niels Leergaard Pedersen)
[1]Present address:Burmeister & Wain Energy A/S, Lundtoftegårdsvej 93A, DK-2800 Kgs. Lyngby, Denmark

cretizations against results from the literature is presented for the benchmarking lid-driven square cavity.

2. Boundary Value Problem

We consider a fluid contained in the domain Ω with boundary $\Gamma \equiv \partial\Omega$, see figure 1. We assume the fluid to be a viscous, incompressible, isothermal, Newtonian fluid, and we furthermore assume it to be stationary. The fluid is then governed by:

$$-\mu\Delta\boldsymbol{u} + \rho\boldsymbol{u}\cdot\nabla\boldsymbol{u} + \nabla p - \rho\boldsymbol{f} = 0 \qquad \text{in } \Omega \tag{1a}$$

$$\nabla\cdot\boldsymbol{u} = 0 \qquad \text{in } \Omega \tag{1b}$$

Equation (1a) is the the steady-state Navier-Stokes equation, expressing conservation of momentum for the fluid and written in the primitive variables p and $\boldsymbol{u}$, where p is pressure and $\boldsymbol{u} = (u_1, u_2)$ is the fluid velocity. The quantities ρ, μ and $\boldsymbol{f}$ denote the density, dynamic viscosity and additional body forces acting on the fluid, respectively. Equation (1b) is the incompressibility condition, and it expresses conservation of mass.

We assume the velocity $\boldsymbol{u}$ to be prescribed along the bondary Γ, and we take the mean pressure to be zero:

$$\boldsymbol{u} = \boldsymbol{u}_D \qquad \text{on } \Gamma \tag{1c}$$

$$\iint_\Omega p \,\mathrm{d}A = 0 \tag{1d}$$

where D in equation (1c) stands for Dirichlet. Other boundary conditions, such as Neumann boundary conditions, could also be considered but have been left out for simplicity.

Numerical methods for solving Navier-Stokes equation (1a) can employ different formulations of the equation. The main results of the present study are based on the *convective* formulation. Comparisons to the *skew-symmetric* formulation are also made, while the *rotational* formulation is left out to avoid the introduction of stabilization [10]. The two formulations differ in their treatment of the non-linear inertial term $\boldsymbol{u}\cdot\nabla\boldsymbol{u}$:

$$(\boldsymbol{u}\cdot\nabla)\boldsymbol{u} \quad \text{or} \quad (\boldsymbol{u}\cdot\nabla)\boldsymbol{u} + \frac{1}{2}\nabla\cdot\boldsymbol{u}. \tag{2}$$

Compared to the convective formulation, the skew-symmetric formulation additionally involves the divergence of the velocity field. Even though these formulations on a continous level are exactly equivalent, due to the incompressibility condition (1b), this is not the case on a discrete level, and therefore the numerical solutions might differ.

3. Isogeometric Method

Equations (1) together comprise the *strong form* of the boundary value problem that governs the state of the fluid. We use NURBS-based isogeometric analysis built on Galerkin's method to solve the problem numerically. This section outlines the procedure. See also [2, 11, 12].

3.1. Geometry Parametrisation

The physical domain Ω is parametrised using NURBS, Non-Uniform Rational B-splines. To make the text self-contained, we very briefly revise the basic concepts of B-splines and NURBS in the following. For a more in-depth treatment of this subject, we refer the reader to e.g. [13].

To define univariate B-splines we choose a polynomial degree $q \in \mathbb{N}$ and a knot vector $\Xi = \{\xi_1, \ldots, \xi_m\}$ with $\xi_i \in \mathbb{R}$ for $i = 1, \ldots, m$. For simplicity, we assume the parametric domain $\xi \in [0, 1]$, and that the knot vector is open such that the boundary knots have multiplicity $q + 1$ with $\xi_1 = \xi_2 = \ldots = \xi_{q+1} = 0$ and $\xi_m = \xi_{m-1} = \ldots = \xi_{m-q} = 1$. The univarite B-splines $\mathcal{N}_i^q : [0; 1] \to \mathbb{R}$ are defined recursively as

$$\mathcal{N}_i^0(\xi) = \begin{cases} 1 & \text{if } \xi_i \le \xi < \xi_{i+1} \\ 0 & \text{otherwise} \end{cases} \tag{3a}$$

for $q = 0$, and

$$\mathcal{N}_i^q(\xi) = \frac{\xi - \xi_i}{\xi_{i+q} - \xi_i}\mathcal{N}_i^{q-1}(\xi) + \frac{\xi_{i+q+1} - \xi}{\xi_{i+q+1} - \xi_{i+1}}\mathcal{N}_{i+1}^{q-1}(\xi) \tag{3b}$$

for $q = 1, 2, \ldots$.

The bivariate tensor product B-splines $\mathcal{P}_{i,j}^{q,r} : [0, 1]^2 \to \mathbb{R}$ are defined from two polynomial degrees q and r and two knot vectors $\Xi = \{\xi_1, \ldots, \xi_m\}$ and $\Phi = \{\phi_1, \ldots, \phi_n\}$:

$$\mathcal{P}_{i,j}^{q,r}(\xi_1, \xi_2) = \mathcal{N}_i^q(\xi_1)\mathcal{M}_j^r(\xi_2), \tag{4}$$

where $\mathcal{N}_i^q$ is the i^{th} univariate B-spline with degree q and knot vector Ξ in the first parametric dimension ξ_1 as defined in equation (3), and $\mathcal{M}_j^r$ is the j^{th} univariate B-spline with degree r and knot vector Φ in the second parametric dimension ξ_2.

The bivariate NURBS $\mathcal{R}_{i,j}^{q,r} : [0, 1]^2 \to \mathbb{R}$ are defined from the NM bivariate B-splines in equation (4) and the weights $W = \{w_{1,1}, \ldots, w_{N,M}\}$ with $w_{i,j} \in \mathbb{R}$ for $i = 1, \ldots, N$ and $j = 1, \ldots, M$:

$$\mathcal{R}_{i,j}^{q,r}(\xi_1, \xi_2) = \frac{w_{i,j}\mathcal{P}_{i,j}^{q,r}}{\sum_{k=1}^{N}\sum_{l=1}^{M} w_{k,l}\mathcal{P}_{k,l}^{q,r}} \tag{5}$$

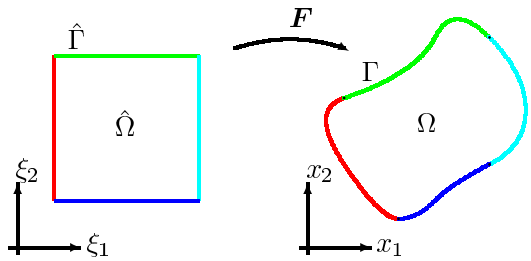

Figure 1: A single patch parametrisation of the fluid domain. Colors indicate how the boundary $\widehat{\Gamma}$ of the parameter domain $\widehat{\Omega}$ is mapped into the boundary Γ of the physical domain Ω.

With the basic concepts of B-splines and NURBS defined, we now make a single patch parametrisation of the fluid domain Ω, see figure 1. We take the parameter domain $\widehat{\Omega}$ as the unit square $(\xi_1, \xi_2) \in [0,1]^2$, and use the bivariate NURBS defined in equation (5). The parametrisation $\boldsymbol{F} : \ [0,1]^2 \to \mathbb{R}^2$ reads:

$$\begin{aligned} \boldsymbol{F}(\xi_1,\xi_2) &= (\ x_1(\xi_1,\xi_2),\ x_2(\xi_1,\xi_2)\ ) \\ &= \sum_{i=1}^{N}\sum_{j=1}^{M} \boldsymbol{d}_{i,j}\mathcal{R}_{i,j}^{q,r}(\xi_1,\xi_2), \end{aligned} \tag{6}$$

where $\boldsymbol{d}_k \in \mathbb{R}^2$ are the control points. By a simple reordering, we can write the above as

$$\boldsymbol{F}(\xi_1,\xi_2) = \sum_{i=1}^{N_{\text{var}}^g} \overline{\boldsymbol{x}}_i \mathcal{R}_i^g(\xi_1,\xi_2), \tag{7}$$

where $N_{\text{var}}^g = NM$ is the number of NURBS, $\overline{\boldsymbol{x}}_i$ are the reordered control points, and $\mathcal{R}_i^g$ are the reordered NURBS. The superscript g indicates that the NURBS functions refer to polynomial degrees, knots vectors and weights that are specific for the geometry representation.

3.2. Field Approximations

In a similar fashion as for the geometry representation in equation (7) above, we seek approximations of the velocity $\boldsymbol{u} : [0;1]^2 \to \mathbb{R}^2$ and pressure $p : [0;1]^2 \to \mathbb{R}$ as linear combinations of the basis functions defined above. Since NURBS are only needed to represent the geometry, and not the velocity and pressure, we will for simplicity use B-splines to approximate the state variables:

$$u_k(\xi_1,\xi_2) = \sum_{i=1}^{N_{\text{var}}^{u_k}} \underline{u}_{ki} \mathcal{P}_i^{u_k}(\xi_1,\xi_2), \tag{8a}$$

$$p(\xi_1,\xi_2) = \sum_{i=1}^{N_{\text{var}}^{p}} \underline{p}_i \mathcal{P}_i^{p}(\xi_1,\xi_2), \tag{8b}$$

where $k = 1, 2$ in (8a) refers to the two components of the velocity field, $\mathcal{P}_i^{u_k}$ denote the B-spline basis functions for the kth component of the velocity field, while $\mathcal{P}_i^p$ similarly denote the B-spline basis functions for the pressure field, all suitably reordered compared to the definition in equation (4). They refer to separate sets of polynomial degrees and knot vectors that are in general not the same. $N_{\text{var}}^{u_k}$ and N_{var}^p are the number of velocity and pressure basis functions, while $\underline{u}_k$ and $\underline{p}$ are the unknown control variables for the velocity and pressure that are to be determined.

The velocity and pressure fields in equations (8) are defined in parameter space, while the governing equations (1) are formulated in physical space. To evaluate the fields in physical space, the inverse of the geometry parametrisation $\boldsymbol{F}$ is used; the pressure $p : \ \Omega \to \mathbb{R}$ over the physical domain is computed as $p \circ \boldsymbol{F}^{-1}$, and the velocity $\boldsymbol{u} : \ \Omega \to \mathbb{R}^2$ over the physical domain as $\boldsymbol{u} \circ \boldsymbol{F}^{-1}$. The Piola mapping could also be used to map the velocity [7], but since none of the examined discretizations are exactly divergent free, we take the simpler approach and map each velocity component as a scalar field. With abuse of notation, we use the same symbol for the state variables both in parameter space and in physical space. Gradients in parameter space, $\widehat{\nabla} p = \left[\frac{\partial p}{\partial \xi_1} \ \frac{\partial p}{\partial \xi_2}\right]^T$, are easily evaluated using the field approximations in equation (8) and the definition of B-splines in equation (4). Gradients in physical space, $\nabla p = \left[\frac{\partial p}{\partial x_1} \ \frac{\partial p}{\partial x_2}\right]^T$, are related to the gradients in parameter space by the formula:

$$\widehat{\nabla} p = \boldsymbol{J}^T \nabla p \iff \nabla p = \boldsymbol{J}^{-T} \widehat{\nabla} p, \tag{9}$$

where $\boldsymbol{J}$ is the Jacobian matrix of the geometry parametrisation:

$$\boldsymbol{J} = \begin{bmatrix} \frac{\partial x_1}{\partial \xi_1} & \frac{\partial x_1}{\partial \xi_2} \\ \frac{\partial x_2}{\partial \xi_1} & \frac{\partial x_2}{\partial \xi_2} \end{bmatrix}, \tag{10}$$

which again is easily evaluated using the mapping in equation (7) and the definitions of NURBS in equation (5).

3.3. Boundary Conditions

For simplicity we impose the Dirichlet boundary conditions in (1c) *strongly* as opposed to the weak enforcement suggested in [14, 15]. Hereby we avoid the need

for definition of penalization parameters which is favorable if a sequence of analysis with different geometries is to performed as in shape optimization problems [16].

In general B-splines have compact support. This means that only a few of the velocity basis functions $\mathcal{P}_i^{u_k}$ in equation (8a) have support on Γ. We can simply arrange the functions $\mathcal{P}^{u_k}$ so that the first $N_{\text{dof}}^{u_k}$ of these do *not* have support on the boundary, and the corresponding control variables of these are thus "degrees of freedom", while the last $N_{\text{fix}}^{u_k} = N_{\text{var}}^{u_k} - N_{\text{dof}}^{u_k}$ *have* support on Γ, and the corresponding control variables are thus "fixed":

$$u_k(\xi_1,\xi_2) = \sum_{i=1}^{N_{\text{dof}}^{u_k}} \underline{u}_{ki}\mathcal{P}_i^{u_k}(\xi_1,\xi_2) + \sum_{i=N_{\text{dof}}^{u_k}+1}^{N_{\text{var}}^{u_k}} \underline{u}_{ki}\mathcal{P}_i^{u_k}(\xi_1,\xi_2). \quad (11)$$

The strong imposition is done by directly specifying suitable values for these last $N_{\text{fix}}^{u_k}$ velocity control variables $\underline{u}_{ki}$, so that the sum in equation (8a) approximates the specified value $\boldsymbol{u}_D$ in (1c). If $\boldsymbol{u}_D$ lies within the function space spanned by $\mathcal{P}_i^{u_k}$, the conditions are satisfied exactly; otherwise they are only satisified in a least square sense.

For the pressure, we note that only the pressure *gradient* appears in the Navier-Stokes equation (1a). The pressure is thus only determined up to an arbitrary constant, which is dealt with by the specification of the mean pressure in equation (1d). Using the approximation in equation (8b), this gives rise to the following equation:

$$\begin{aligned} 0 &= \iint_\Omega p\,\mathrm{d}A = \iint_\Omega \sum_{i=1}^{N_{\text{var}}^p} \underline{p}_i \mathcal{P}_i^p(x_1,x_2)\,\mathrm{d}x_1\,\mathrm{d}x_2 \\ &= \sum_{i=1}^{N_{\text{var}}^p} \underline{p}_i \int_0^1\int_0^1 \mathcal{P}_i^p(\xi_1,\xi_2)\det(\boldsymbol{J})\,\mathrm{d}\xi_1\,\mathrm{d}\xi_2 = \underline{\boldsymbol{p}}\boldsymbol{M}^T, \quad (12) \end{aligned}$$

where $\underline{\boldsymbol{p}}$ is the vector of pressure control variables, $\boldsymbol{M}$ the vector of integrals of pressure basis functions, and $\boldsymbol{J}$ is given by (10). Since no pressure control variables needs to be fixed, we have $N_{\text{dof}}^p = N_{\text{var}}^p$ and $N_{\text{fix}}^p = 0$.

3.4. Weak Form of the Governing Equations

The governing equations (1) are cast into their *weak*, or *variational*, form. For this we use the (image in physical space of the) B-spline introduced above as *weight functions* for the governing equations. We will use only the first $N_{\text{dof}}^{u_k}$ velocity basis functions, since these have no support on the fixed boundary. We multiply the kth component of the Navier-Stokes equation (1a) by an arbitrary weight function $\mathcal{P}_i^{u_k}$ among these velocity basis functions, and the incompressibility equation (1b) by an arbitrary weight function $\mathcal{P}_j^p$ among the pressure basis functions, integrate the resulting equations over Ω, and then simplify using integration by parts. After some manipulations we find the following weak form of the governing equations:

$$\begin{aligned} 0 = \iint_\Omega \Big(&(\mu\nabla\mathcal{P}_i^{u_k} + \rho\mathcal{P}_i^{u_k}\boldsymbol{u})\cdot\nabla u_k \\ &- (p\nabla\mathcal{P}_i^{u_k} + \rho\mathcal{P}_i^{u_k}\boldsymbol{f})\cdot\boldsymbol{e}_k\Big)\,\mathrm{d}x_1\,\mathrm{d}x_2 \quad (13a) \\ 0 = \iint_\Omega \mathcal{P}_j^p\,(\nabla\cdot\boldsymbol{u})\,\mathrm{d}x_1\,\mathrm{d}x_2 \quad (13b) \end{aligned}$$

for $k = 1,2$, $i = 1,\ldots,N_{\text{dof}}^{u_k}$ and $j = 1,\ldots,N_{\text{dof}}^p$, and where $\boldsymbol{e}_k$ is the k^{th} unit vector.

3.5. Matrix Equation

Finally, we insert the (image in physical space of the) approximations of the velocity and pressure fields (8) into the weak form (13) of the governing equations, split the superpositions of $\boldsymbol{u}$ into parts with support on the fixed boundary and parts without as in equation (11), exchange the order of summation and integration, rearrange to get the unknown terms on the LHS and the known terms on the RHS, and pull the integration back to parameter space using standard transformation rules for multiple integrals along with equation (9). This gives:

$$\begin{aligned} &\overbrace{\begin{bmatrix} \boldsymbol{K}_1+\boldsymbol{C}_1(\bar{\boldsymbol{u}}) & \boldsymbol{0} & -\boldsymbol{G}_1^T \\ \boldsymbol{0} & \boldsymbol{K}_2+\boldsymbol{C}_2(\bar{\boldsymbol{u}}) & -\boldsymbol{G}_2^T \\ \boldsymbol{G}_1 & \boldsymbol{G}_2 & \boldsymbol{0} \end{bmatrix}}^{\overline{\boldsymbol{M}}(\overline{\boldsymbol{U}})} \overbrace{\begin{bmatrix} \bar{\boldsymbol{u}}_1 \\ \bar{\boldsymbol{u}}_2 \\ \bar{\boldsymbol{p}} \end{bmatrix}}^{\overline{\boldsymbol{U}}} \\ &= \underbrace{\begin{bmatrix} \boldsymbol{f}_1 \\ \boldsymbol{f}_2 \\ \boldsymbol{0} \end{bmatrix} - \begin{bmatrix} \boldsymbol{K}_1^\star+\boldsymbol{C}_1^\star(\bar{\boldsymbol{u}}) & \boldsymbol{0} \\ \boldsymbol{0} & \boldsymbol{K}_2^\star+\boldsymbol{C}_2^\star(\bar{\boldsymbol{u}}) \\ \boldsymbol{G}_1^\star & \boldsymbol{G}_2^\star \end{bmatrix}\begin{bmatrix} \bar{\boldsymbol{u}}_1^\star \\ \bar{\boldsymbol{u}}_2^\star \end{bmatrix}}_{\overline{\boldsymbol{F}}}, \end{aligned} \quad (14)$$

or simply $\overline{\boldsymbol{M}}(\overline{\boldsymbol{U}})\,\overline{\boldsymbol{U}} = \overline{\boldsymbol{F}}$, with

$$\underline{K}_{ijk} = \mu \int_0^1\int_0^1 \left(\boldsymbol{J}^{-T}\nabla\mathcal{P}_i^{u_k}\right)\cdot\left(\boldsymbol{J}^{-T}\nabla\mathcal{P}_j^{u_k}\right)\det(\boldsymbol{J})\,\mathrm{d}\xi_1\,\mathrm{d}\xi_2, \tag{15a}$$

$$\underline{C}_{ijk}(\underline{\boldsymbol{u}}) = \rho \int_0^1\int_0^1 \mathcal{P}_i^{u_k}\left(\boldsymbol{u}(\underline{\boldsymbol{u}}_i)\cdot(\boldsymbol{J}^{-T}\nabla\mathcal{P}_j^{u_k})\right)\det(\boldsymbol{J})\,\mathrm{d}\xi_1\,\mathrm{d}\xi_2, \tag{15b}$$

$$\underline{G}_{ijk} = \int_0^1\int_0^1 \mathcal{P}_i^{p}\left(\boldsymbol{J}^{-T}\nabla\mathcal{P}_j^{u_k}\right)\cdot\boldsymbol{e}_k\det(\boldsymbol{J})\,\mathrm{d}\xi_1\,\mathrm{d}\xi_2, \tag{15c}$$

$$f_{ik} = \rho \int_0^1\int_0^1 \mathcal{P}_i^{u_k}\left(\boldsymbol{f}\cdot\boldsymbol{e}_k\right)\det(\boldsymbol{J})\,\mathrm{d}\xi_1\,\mathrm{d}\xi_2, \tag{15d}$$

$$\underline{\boldsymbol{K}}_k = \begin{bmatrix} \boldsymbol{K}_k & \boldsymbol{K}_k^{\star} \end{bmatrix} \quad (N_{\mathrm{dof}}^{u_k}\times(N_{\mathrm{dof}}^{u_k}+N_{\mathrm{fix}}^{u_k})). \tag{15e}$$

$$\underline{\boldsymbol{C}}_k(\underline{\boldsymbol{u}}) = \begin{bmatrix} \boldsymbol{C}_k(\underline{\boldsymbol{u}}) & \boldsymbol{C}_k^{\star}(\underline{\boldsymbol{u}}) \end{bmatrix} \quad (N_{\mathrm{dof}}^{u_k}\times(N_{\mathrm{dof}}^{u_k}+N_{\mathrm{fix}}^{u_k})). \tag{15f}$$

$$\underline{\boldsymbol{G}}_k = \begin{bmatrix} \boldsymbol{G}_k & \boldsymbol{G}_k^{\star} \end{bmatrix} \quad (N_{\mathrm{dof}}^{p}\times(N_{\mathrm{dof}}^{u_k}+N_{\mathrm{fix}}^{u_k})), \tag{15g}$$

where $k = 1, 2$, $\boldsymbol{J}$ is the Jacobian matrix in equation (10), $\boldsymbol{u}(\underline{\boldsymbol{u}})$ is given by the approximation in equation (8), $\boldsymbol{e}_k$ is the k^{th} unit vector, $\underline{\boldsymbol{u}}_k^T = [\overline{\boldsymbol{u}}_k^T\,\overline{\boldsymbol{u}}_k^{\star T}]$, and all starred quantities are given by the boundary conditions. $\boldsymbol{K}_k$ is often called viscosity matrix, $\boldsymbol{C}_k$ convective matrix, $\boldsymbol{G}_k$ gradient matrix, and $\boldsymbol{f}_k$ force vector.

The integrals in equation (15) are evaluated using Gaussian quadrature. The necessary number of quadrature points N_G in each knot span is estimated from the relation $\tilde{q} = 2N_G - 1$, where $\tilde{q}$ is an estimate of the highest polynomial degree of the integrands. Since the integrands are in general rational functions, we simply estimate $\tilde{q}$ as the sum of polynomial degrees of the numerator and the denominator. Using polynomial degree 2 for the geometry and 4 for the velocity and pressure, we estimate a polynomial degree of $\tilde{q} = 12$ for the integrand of $\boldsymbol{C}$, and this dictates that we should use at least $N_G = 7$ quadrature points in each knot span. All results in the following are based on 7 quadrature points per knot span, which is a conservative choice compared to recent studies on more efficient quadrature rules [17].

We need to solve $N_{\mathrm{dof}}^{u_1} + N_{\mathrm{dof}}^{u_2} + N_{\mathrm{dof}}^{p}$ equations from (14) supplemented by the equation from the condition on the mean pressure from (12) in $N_{\mathrm{dof}}^{u_1} + N_{\mathrm{dof}}^{u_2} + N_{\mathrm{dof}}^{p}$ unknowns, and we do this in the least square sense. The problem is non-linear, and an incremental Newton-Raphson method is used by gradually increasing *Re*, see e.g. [11].

4. Stability for Stokes Problem:Wall-Driven Anullar Cavity

In the following section, we deal with the stability of the isogeometric method when applied to Stokes flow, which is the problem that arises when we neglect the non-linear inertial term in Navier-Stokes equation (1a). Some discretizations of the mixed formulation of Stokes problem are stable while others are unstable. Unstable discretizations can leave the system matrix $\overline{\boldsymbol{M}}$ in equation (14) singular or badly scaled, which in turn leads to spurious, unphysical oscillations for the pressure field, while the velocity field may still look quite reasonable. Figure 3 below shows an example of this. Furthermore, it deteriorates the convergence properties of the method and thus prohibits iterative solutions for the full Navier-Stokes problem. In order for a given discretization to be stable, it needs to satisfy the socalled inf-sup condition, also known as the BB or LBB condition:

$$\inf_p \sup_{\boldsymbol{u}} \frac{\int_\Omega p\nabla\cdot\boldsymbol{u}\,\mathrm{d}A}{\|p\|\,\|\boldsymbol{u}\|} \geq \beta > 0, \tag{16}$$

where the positive constant β is independent of the mesh. In equation (16), the norm of p is the L^2-norm, while the norm of $\boldsymbol{u}$ is the H^1-norm.

In this section we study how stable discretizations may be constructed by using different basis functions for the velocity and pressure fields. More specifically, we will establish suitable choices of polynomial degrees and knot vectors for the velocity and pressure such that the discretizations are stable. This idea follows the approach in a recent work [7], in which three families of stable discretizations were presented, but contrasts to the stabilized method in which identical basis functions for the velocity and pressure may be used on the cost that stabilizing terms must be added to the Stokes equation, see e.g. [3].

We report the stability of the isogeometric discretizations listed in table 1. The discretizations differ in polynomial degrees, knot refinements and inner knot multiplicities between the velocity and pressure representations. We have adobted a heuristic nomenclature for naming of the individual discretizations. For the $\mathbf{u}4_0^2\mathrm{p}3_0^1$ discretization (d), e.g., both velocity components are approximated using quartic B-splines ($\mathbf{u}4$), and the pressure using cubic B-splines (p3). Superscript indicates the multiplicity of inner knots, and thus also the degree of continuity across knots, since this is just the degree minus the multiplicity. Subscript indicates the number of *h*-refinements by halfing all knot spans. For the strategies a-g, each of the velocity componenents u_1 and

	Name	Knot Vector 1	Knot Vector 2	inf-sup
a	$\mathbf{u}4^1_1\mathrm{p}4^1_0$	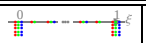	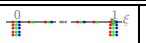	√
b	$\mathbf{u}4^2_0\mathrm{p}4^1_0$	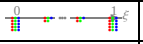	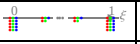	√
c	$\mathbf{u}4^1_1\mathrm{p}3^1_0$	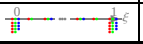	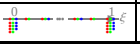	√
d	$\mathbf{u}4^2_0\mathrm{p}3^1_0$	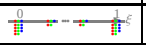	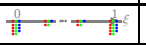	√
e	$\mathbf{u}4^1_1\mathrm{p}2^1_0$	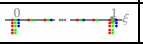	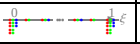	√
f	$\mathbf{u}4^2_0\mathrm{p}2^1_0$	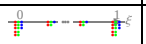	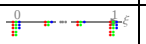	√
g	$\mathbf{u}4^1_0\mathrm{p}2^1_0$	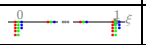	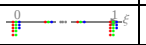	÷
h	Nédélec	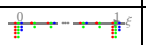	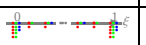	√
i	Raviart-Thomas	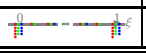	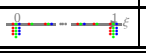	√

Table 1: Discretization names, knot vectors and inf-sup-stability. Velocity knot vectors are shown in red and green, while the pressure knot vector is shown in blue.

u_2 are represented identically, which reduces the computational expenses since equality of the basis functions $\mathcal{R}_i^{u_1} = \mathcal{R}_i^{u_2}$ implies equality of the matrices $K_{ij1} = K_{ij2}$, and in addition all fields are represented identically in both parametric directions. This is not the case for the strategies h and i, which are modified versions of the Nédélec and Raviart-Thomas elements presented in [7]. Compared to the original formulation in [7], the velocity fields have been *h*-refined once. It should be stressed that with this enlargement of the velocity space, the exact fulfillment of the divergence-free constraint for the Raviart-Thomas discretization is lost. The $\mathbf{u}4^2_0\mathrm{p}3^1_0$ discretization (d) was originally proposed in [3] and subsequently introduced in [7] as the Taylor-Hood element.

To examine the numerical stability, we consider the wall-driven annular cavity problem outlined in figure 2**a**. This is a slight modification of the standard benchmark *lid*-driven *square* cavity problem, see the treatment of the problem in Section 6, utilizing the capability of isogeometric analysis to exactly represent circular arcs. The fluid is contained in an annular cavity. The inner circular wall moves with constant tangential speed, while the remaining three walls are at rest. The velocity field is specified along the boundary of the domain, assuming no-slip conditions. No body forces act upon the fluid, and the fluid motion is thus caused—or driven—by the moving wall. We adopt the so-called *leaky-lid* boundary condition, meaning that the corners $(x, y) = (0, 1)$ and $(x, y) = (1, 0)$ belong to the moving wall boundary. We parametrise the domain using quadratic NURBS. The control net is shown in figure 2**b**, and the data for the geometry parametrisation are

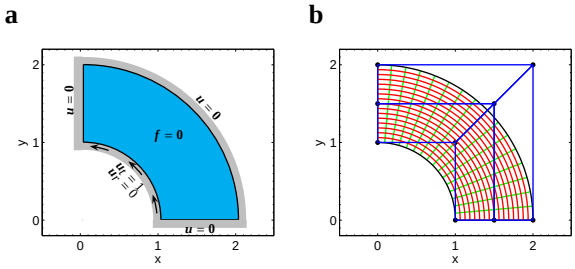

Figure 2: Driven annular cavity. **a**: Domain and boundary conditions. **b**: Control net (black dots and blue lines) and image of the computational mesh for velocity and pressure (red and green lines).

listed in table A.2 in Appendix Appendix A. For the velocity and pressure representation, we *h*-refine the parameter mesh for the geometry by halfing the knot spans, leading to a familiy of parameter meshes ranging from 2×2 to 64×64 knot spans, one of which is also depicted in figure 2**b**.

Figure 3 shows the computed velocity and pressure fields for two different discretizations, namely the $\mathbf{u}4^1_0\mathrm{p}4^1_0$ discretization (top row) and the $\mathbf{u}4^1_1\mathrm{p}4^1_0$ discretization (bottom row). Both of these produce a reasonable, rotational flow field. Clear pressure oscillations, however, are seen for first discretization, whereas the latter nicely approximates the pressure singularitites in the inner corners.

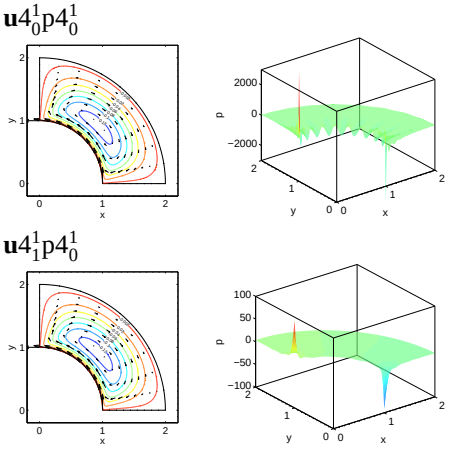

Figure 3: Computed fields for $\mathbf{u}4^1_0\mathrm{p}4^1_0$ (top) and $\mathbf{u}4^1_1\mathrm{p}4^1_0$ (bottom) discretizations. Left: stream function contour lines and velocity arrows. Right: pressure (note the different vertical scalings).

To test the stability of the discretization strategies, we use the approach described in [18, 19]. For each discretization, we vary the grid size for the velocity and

pressure representations, and for each of these meshes we determine a numerical estimate of the inf-sup "constant" β in equation (16). If this value does not change appreciably with varying grid size, it indicates that the discretization is stable. On the other hand, if the value tends to zero as the grid size changes, it indicates that the discretization is *un*stable.

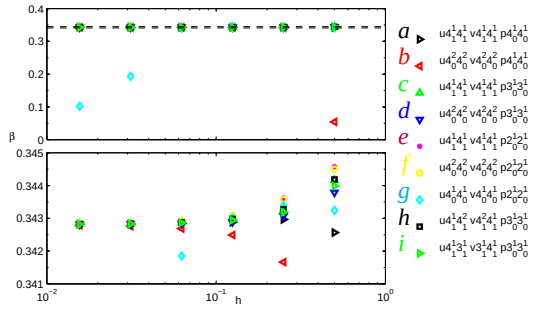

Figure 4: Numerically computed inf-sup "constants" for varying grid size using different discretizations. The bottom plot shows an enlargement of the top plot as marked by the dashed lines.

The results of these computations are shown in figure 4. From this we are led to conclude, that the discretization with identical polynomial degree for velocity and pressure is stable if either the velocity knot vector is refined (a) or the inner knot multiplicity for the velocity is increased (b). The same conclusion applies to the discretizations for which the polynomial degree of the velocity is larger than the polynomial degree of the pressure by one (c and d) and two (e and f). The stability of $\mathbf{u}4_0^2\mathrm{p}3_0^1$ (d) was already known from [7]. Both the modified Nédélec (h) and Raviart-Thomas (i) discretizations are seen to be stable, whereas the simple discretization $\mathbf{u}4_0^1\mathrm{p}2_0^1$ (g) with a difference in polynomial degree of two but with identical inner knots does *not* pass the stability test. The stability of each of the discretizations is summarized in the right-most column of table 1.

Several discretizations have been tested in addition to those listed in table 1. It was found that increasing the difference between the polynomial degree of the velocity approximation and the degree of the pressure approximation does influence the inf-sup stability, even without inserting or repeating knots. More specifically, the value of grid size h where the inf-sup "constant" β starts decreasing seemed to decrease with increasing polynomial degrees.

Assuming that the examined discretizations are representative, two simple strategies for choosing stable discretizations for the velocity and pressure approximations can be established by means of induction. Given a simple discretization for the pressure, i.e. open knot vectors, choose the velocity degrees at least equal to the pressure degree and then either take the velocity knot vectors as the refinement of the pressure knot vectors, or use the pressure knot vectors with all inner knots repeated. Or conversely, given simple discretizations for the velocity, i.e. with open knot vectors and single or double inner knots, choose the pressure degree less than or equal to the velocity degree, and take the pressure knot vectors as the velocity knot vectors with every 2nd inner knot removed. The knot refinement strategy is used for the cases a, c and e, and the knot repetition strategy for cases b, d and f. The modified Raviart-Thomas (i) also uses the refinement strategy, while the modified Nédélec (h) combines both strategies.

We should emphasize firstly that the presented inf-sup method only serves as a numerical test of the stability of the examined discretizations, and secondly that the inductive step, going from the stability of the examined discretizations to the stability of a general discretization strategy, is only motivated by a limited number of tests. None of these should in no way be mistaken for a rigorous mathematical proof.

5. Error Convergence: Forced Elliptic Cavity

To asses the validity of the isogeometric method for the full Navier-Stokes problem, we consider a test case for which an analytical solution exists, and examine how well the discretizations listed in table 1 are able to reproduce the exact solution.

The problem is outlined in figure 5**a**. We take the physical domain Ω as the elliptic disk $\{(x_1, x_2) \in \mathbb{R}^2 \mid (x_1/a)^2 + (x_2/b)^2 \leq 1\}$ with $a = 2$ and $b = 1$. Assuming appropriate units are assigned to all quantities and focussing only on their numerical values, we set $\rho = \mu = 1$, take the body force $\boldsymbol{f} = (f_1, f_2)$ to be

$$
\begin{aligned}
f_1 = &-\frac{1}{4}U^2 \sin^2\left(\pi\tilde{r}^2\right) x - \frac{1}{4}\frac{\pi}{\tilde{r}} \sin\left(\pi\tilde{r}\right) x + \frac{13}{2}\pi U \cos\left(\pi\tilde{r}^2\right) y \\
&- 4\pi^2 U \sin\left(\pi\tilde{r}^2\right) y^3 - \frac{1}{4}\pi^2 U \sin\left(\pi\tilde{r}^2\right) x^2 y \\
f_2 = &-\frac{1}{4}U^2 \sin^2\left(\pi\tilde{r}^2\right) y - \frac{\pi}{\tilde{r}} \sin\left(\pi\tilde{r}\right) y - \frac{7}{8}\pi U \cos\left(\pi\tilde{r}^2\right) x \\
&+ \frac{1}{16}\pi^2 U \sin\left(\pi\tilde{r}^2\right) x^3 + \pi^2 U \sin\left(\pi\tilde{r}^2\right) y^2 x,
\end{aligned}
$$

where $\tilde{r} = \tilde{r}(x, y) = \sqrt{(x/2)^2 + y^2}$, and assume no-slip boundary conditions: $\boldsymbol{u} = \mathbf{0}$ on Γ. The following velocity and pressure fields solve the governing equations

and satisfy the boundary conditions:

$$
\begin{aligned}
u_1^\star &= -U \sin(\pi \tilde{r}^2)\, y, \\
u_2^\star &= \frac{1}{4} U \sin(\pi \tilde{r}^2)\, x, \\
p^\star &= \frac{4}{\pi^2} + \cos(\pi \tilde{r}),
\end{aligned}
$$

where U is a velocity scale which in the following is assumed to be $U = 200/\sqrt{5}$. These fields are depicted in figure 5**b**-**c**. Using $L = \sqrt{a^2 + b^2} = \sqrt{5}$ as length scale, the Reynolds number for the problem is $Re = 200$ which makes the problem weakly nonlinear. We parametrise

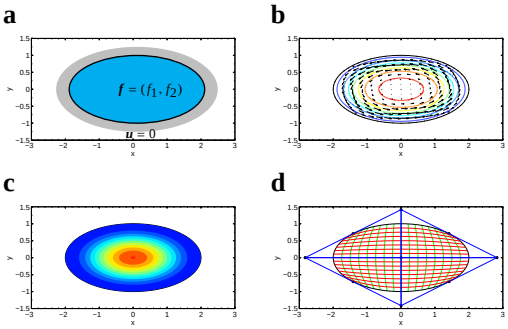

Figure 5: Forced elliptic cavity. **a**: Domain and boundary conditions. **b**: Analytical stream function contour lines and velocity arrows. **c**: Analytical pressure contour lines. **d**: Control net (black dots and blue lines) and image of the coarsest computational mesh for velocity and pressure (red and green lines).

the domain using quadratic NURBS. The control net and the coarsest computational mesh for the velocity and pressure fields are shown in figure 5**d**.

We examine how well the exact velocity and pressure fields are reproduced by a given discretization as the computational parameter mesh is *h*-refined by knot insertion. For each discretization we uniformly vary the computational mesh for velocity and pressure in the range from 4×4 to 64×64 knot spans, and for each of these meshes we compute the L^2-norm and the H^1-seminorm of the velocity residual and the pressure residual as measures of the error:

$$
\begin{aligned}
\epsilon_u^2 &= \iint_\Omega \|\boldsymbol{u}(x_1, x_2) - \boldsymbol{u}^\star(x_1, x_2)\|^2 \mathrm{d}x_1 \mathrm{d}x_2, \\
\epsilon_p^2 &= \iint_\Omega |p(x_1, x_2) - p^\star(x_1, x_2)|^2 \mathrm{d}x_1 \mathrm{d}x_2, \\
\epsilon_{\nabla u}^2 &= \iint_\Omega \sum_{k=1}^{2} \|\nabla u_k(x_1, x_2) - \nabla u_k^\star(x_1, x_2)\|^2 \mathrm{d}x_1 \mathrm{d}x_2, \\
\epsilon_{\nabla p}^2 &= \iint_\Omega \|\nabla p(x_1, x_2) - \nabla p^\star(x_1, x_2)\|^2 \mathrm{d}x_1 \mathrm{d}x_2.
\end{aligned}
$$

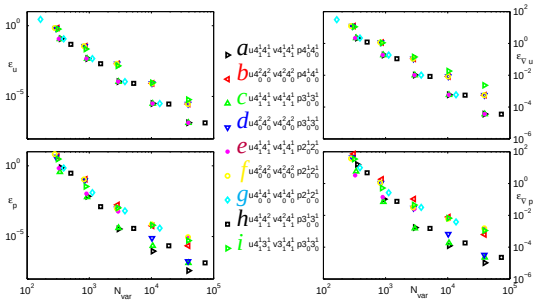

Figure 6: Convergence of error: L^2-norm (left) and H^1-seminorm (right) of velocity residual (top) and pressure residual (bottom) as function of the total number of variables of the analysis using different discretizations.

The results are shown in figure 6. The figure depicts the velocity error (top) and pressure error (bottom) as function of the total number of variables of the analysis, using both the L^2-norm (left) and the H^1-seminorm (right). We note that the discretizations a-f which pairwise have identical polynomial degrees, the knot refinement strategies (a, c, e) have a significantly lower velocity error than the knot repetion strategies (b, d, f). In addition, the difference between the two strategies grows as the number of degrees of fredoom increases, as is most evident for the H^1-seminorm. The difference in pressure error between the two strategies varies more, but the error of the knot refinement strategy is never larger than the error of the corresponding knot repetion strategy. This make the knot refinement strategy favorable in a per-degree-of-freedom sense. The knot refinement strategy, unlike the knot repetition strategy, conserves the degree of continuity for the velocity field. This therefore confirms the high importance of continuity alluded to in [4]. However, although the increase in number of degrees of freedom for a given refinement is nearly identical for the two strategies, the knot refinement strategy is computationally more expensive than

the knot repetition strategy, since it doubles the number of knot spans and thus quadruples the number of function evaluations needed for the Gaussian quadrature, unless more efficient quadrature rules are employed [17]. It is also worth noting that although the pressure error of the unstable discretization $\mathbf{u}4_0^1\mathrm{p}2_0^1$ (g) flattens out quit quickly as the number of degrees of freedom increases, the velocity error falls off impressively. Lastly, the modified Raviart-Thomas discretization (h) seem to perform somewhat better than the modified Nédélec discretization (i) for both the velocity and the pressure.

We have in general good experiences with the Taylor-Hood discretization $\mathbf{u}4_0^2\mathrm{p}3_0^1$ (d), since it discretizes both velocity components identically, and the knot spans for the velocity and pressure fields are also the same. We therefore base the following examination of the influence of the formulations of the Navier-Stokes equation on this discretization. We solve the problem outlined above using both the convective formulation as above and the skew-symmetric formulation, and we do this for two different values of the Reynolds number, namely 200 and 2,000, using {400; 800; 1,000; 1,500} as intermediate values to ensure convergence. Figure 7 compares the convergence of errors for the two formulations. For the low Reynolds number, both the velocity

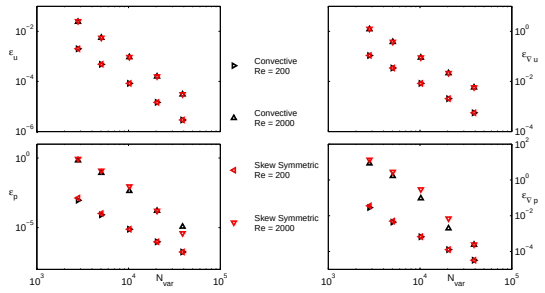

Figure 7: Convergence of error: L^2-norm (left) and H^1-seminorm (right) of velocity residual (top) and pressure residual (bottom) as function of the total number of variables of the analysis for different formulations and Reynolds numbers using the discretization $\mathbf{u}4_0^2\mathrm{p}3_0^1$ (d).

and the pressure errors of the two formulations are practically identical. For the higher Reynolds number, some differences are seen for the pressure error, while the velocity errors remain similar. It should also be mentioned that in our experience, more non-linear solver iterations are needed for the skew-symmetric formulation to converge compared to the convective formulation.

6. Benchmark: Lid-Driven Square Cavity

As a final validation of the isogeometric method, we compare our results for a standard benchmark flow problem, namely the lid-driven square cavity [12, 3], against results from other numerical simulations [20, 21, 22]. We consider a fluid contained in a square cavity with the top wall moving with constant speed, and the other walls kept still as outlined in figure 8**a**. This prescribes the velocity field along the boundary of the domain, assuming no-slip conditions at the walls and closed-lid conditions ($\boldsymbol{u} = \mathbf{0}$) at the upper corners. No body forces act upon the fluid; the fluid is set in motion from the movement of the lid. We parametrise the domain using linear NURBS, and construct a stretched computational mesh with increased resolution around the corner singularities and boundary regions, see figure 8**b**. For the analysis, a computational grid of 64×64 regularly spaced knot spans is employed.

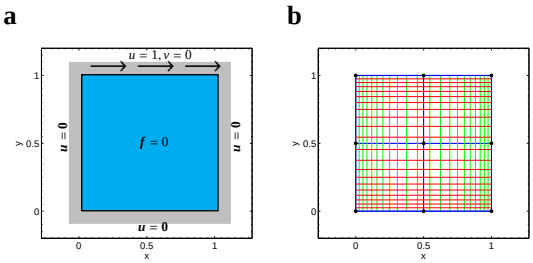

Figure 8: Lid-driven square cavity. **a**: Domain and boundary conditions. **b**: Control net (black dots and blue lines) and image of regularly spaced isoparametric lines (red and green lines).

Using the isogeometric discretizations listed in table 1 we firstly solve the problem for Reynolds number $Re = 5{,}000$. We gradually increase Re, and the number of intermediate steps in Re necessary to achieve convergence for $Re = 5{,}000$ is around five, but is in general different for the various discretizations. The total number of basis functions for the analysis ranges from 13,604 for the discretization $\mathbf{u}4_0^1\mathrm{p}2_0^1$ (g) to 72,865 for the Nédélec discretization (h), while the remaining discretizations all have between 38,678 and 39,472 analysis basis functions. Figure 9 compares the computed horizontal/vertical velocity profiles through the vertical/horizontal center line of the cavity to the data from [20]. On the left, the velocity profiles for all nine discretizations are seen to match very well with the data in [20]. On the right, the velocity residuals reveal that all discretizations yield slightly larger fluid speeds away from the center and towards the boundaries compared

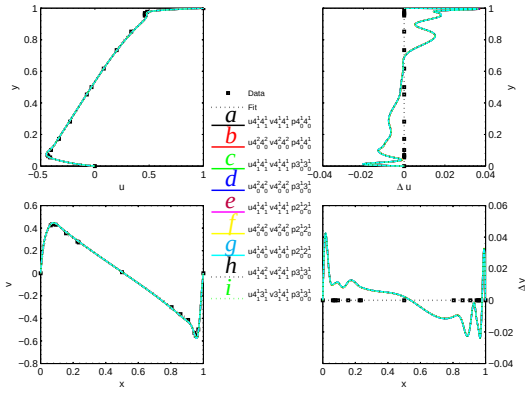

Figure 9: Comparison of velocity profile curves and residual curves (velocity minus fit) for the lid-driven square cavity for Re = 5,000 using different discretizations, plotted with data from [20] and a fit to the data using a cubic spline. Top: horizontal velocity profiles (left) and residuals (right) through the vertical center line. Bottom: vertical velocity profiles (left) and residuals (right) through the horizontal center line.

to the data. The agreement between the discretizations, however, is very good.

In the following, we once again focus on the discretization $\mathbf{u}4_0^2\mathrm{p}3_0^1$ (d). Figure 10 shows velocity vectors and stream function contour lines for Re = 5,000. The

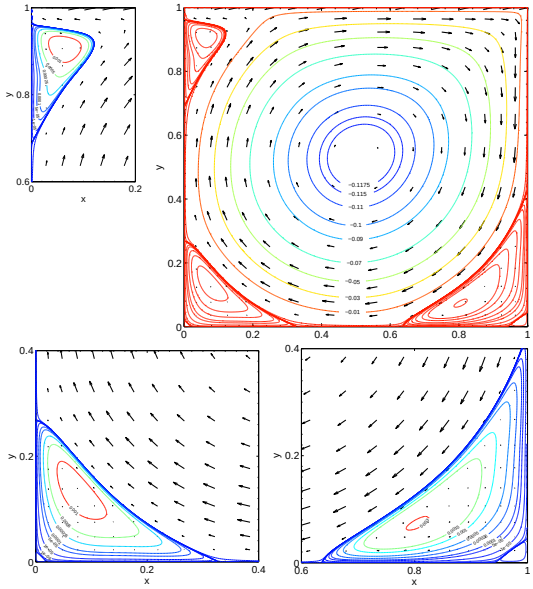

Figure 10: Four views of velocity vectors and stream function contour lines in the lid-driven square cavity for Re = 5,000 using the $\mathbf{u}4_0^2\mathrm{p}3_0^1$ discretization (d).

general pattern of the stream function matches very well with the results of [20], [21] and [22]. The locations and the extremal values of both the central main eddy as well as the minor eddies in the bottom right, bottom left and top left corners are in overall agreement. Small discrepencies are still seen, e.g. close to the boundary in the top left corner.

Finally, the problem is solved for different values of Re in the range from 100 to 10,000: {*100*; *400*; *1,000*; 2,000; *3,200*; *5,000*; *7,500*; *10,000*}. Figure 11**a/b** shows the computed horizontal/vertical velocity profiles through the vertical/horizontal center line of the cavity along with the data from [20] for the values of Re printed in italic. In general, the velocity profiles from

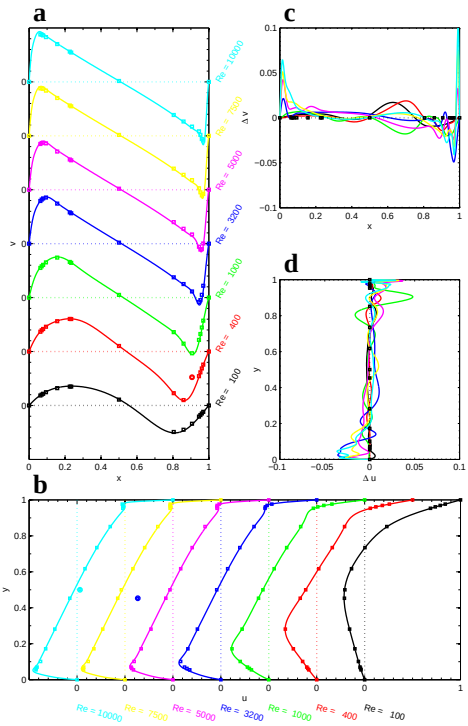

Figure 11: Velocity profile curves for the lid-driven square cavity for seven values of Re (solid lines) using the $\mathbf{u}4_0^2\mathrm{p}3_0^1$ discretization (d) plotted along with data from [20] (points). **a**: vertical velocity profile through the horizontal center line. **b**: horizontal velocity profile through the vertical center line. **c**: vertical velocity residual. **d**: horizontal velocity residual. The profile curves have been translated to avoid clustering of data. We speculate that three obvious outliers, marked with rings, stem from misprints in the tabulated data in [20]. Cubic splines have been fitted to the remaining data.

the present study match very well with the data in [20]. Once again, however, a closer examination reveals a small difference: for higher Re, we compute slightly larger fluid speeds close to the boundaries than is done in [20], and this difference increases with Re. There is, however, a very nice agreement in the location of the

velocity extrema.

Regarding the differences in flow speeds close to the boundaries, several points deserve mentioning. Firstly, the results depend critically on the choice of boundary conditions specified for the upper corners. We emphasize that closed-lid conditions are assumed in the present study. Secondly, the results depend slightly on the formulation of the Navier-Stokes equation (1a) for $Re \gtrsim 5{,}000$, depending on whether the convective or the skew-symmetric formulation is used. This is shown in figure 12, where the computed velocity profiles using each of the two different formulations are compared for $Re = 10{,}000$. The convective and the skew-symmetric

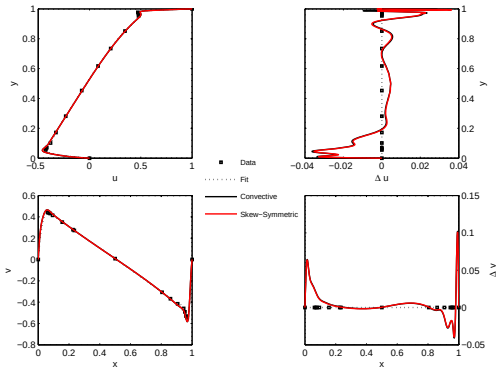

Figure 12: Comparison of velocity profile curves and residual curves (velocity minus fit) for the lid-driven square cavity for $Re = 10{,}000$ with different formulations of the inertial term using the $\mathbf{u}4_0^2\mathrm{p}3_0^1$ discretization (d), plotted with data from [20] and a fit to the data using a cubic spline. Top: horizontal velocity profiles (left) and residuals (right) through the vertical center line. Bottom: vertical velocity profiles (left) and residuals (right) through the horizontal center line.

formulations are found to nearly match each other in the interior, whereas some differences are observed close to the boundaries, in particular at the moving lid. We emphasize that the present study is based on the simpler convective formulation of the Navier-Stokes equation. Thirdly, the data in [20] are relatively sparse at the boundaries where the variation in velocity is high. Finally, it should be stressed that the data in [20] stem from another numerical study, and an exact correspondence between that and the present study should not be expected.

7. Conclusions

This paper has examined various discretizations in isogeometric analysis of 2-dimensional, steady state, incompressible Navier-Stokes equation subjected to Dirichlet boundary conditions. Firstly, a detailed description of the implementation has been given. Secondly, numerical inf-sup stability tests have been presented that confirm the existence of many stable discretizations of the velocity and pressure spaces. In particular it was found that stability may be achieved by means of knot refinement of the velocity space. Thirdly, error convergence studies compared the performance of the various discretizations and indicated optimal convergence, in a per-degree-of-freedom sense, of the discretization with identical polynomial degrees of the velocity and pressure spaces but with the velocity space enriched by knot refinement. Finally, the method has been applied to the lid-driven square cavity for benchmarking purposes, showing that the stable discretizations produce consistent results that match well with existing data and thus confirm the robustness of the method.

Appendix A. Data for Geometry Parametrisations

Table A.2 lists the polynomial degrees, knot vectors and control points for the geometry of the analysed problems.

References

[1] T. Hughes, J. Cottrell, Y. Bazilevs, Isogeometric analysis: CAD, finite elements, NURBS, exact geometry and mesh refinement, Comput. Methods Appl. Mech. Engrg. 194 (2005) 4135–4195.

[2] J. Cottrell, T. Hughes, Y. Bazilevs, Isogeometric Analysis: Toward Integration of CAD and FEA, John Wiley and Sons, 2009.

[3] Y. Bazilevs, L. D. Veiga, J. Cottrell, T. Hughes, G. Sangalli, Isogeometric analysis: Approximation, stability and error estimates for *h*-refined meshes, Mathematical Models and Methods in Applied Science 16 (2006) 1031–1090.

[4] I. Akkerman, Y. Bazilevs, V. Calo, T. Hughes, S. Hulshoff, The role of continuity in residual-based variational multiscale modeling of turbulence., Comput. Mech. 41 (2010) 371–378.

[5] Y. Bazilevs, T. Hughes, NURBS-based isogeometric analysis for the computation of flows about rotating components, Comput. Mech. 43 (2008) 143–150.

[6] Y. Bazilevs, I. Akkerman, Large eddy simulation of turbulent taylor-couette flow using isogeometric analysis and the residual-based variational multiscale method, Journal of Computational Physics 229 (2010) 3402–3414.

[7] A. Buffa, C. de Falco, G. Sangalli, Isogeometric Analysis: Stable elements for the 2D stokes equation, Int. J. Numer. Meth. Fluids (2011).

[8] A. Bressan, Isogeometric regular discretization for the Stokes problem, IMA Journal of Numerical Analysis2 (2010).

[9] A. Bressan, Personal communication.

[10] W. Layton, C. Manica, M. Neda, M. Olshanskii, L. Rebholz, On the accuracy of the rotation form in simulations of the Navier-Stokes-equations, Journal of Computational Physics 228 (2009) 3433–3447.

[11] J. Reddy, D. Gartling, The finite element method in heat transfer and fluid dynamics, CRC Press, 2nd edition, 2001.

[12] J. Donea, A. Huerta, Finite Element Methods for Flow Problems, John Wiley and Sons, 2003.
[13] L. Piegl, W. Tiller, The NURBS Book, Springer, 1995.
[14] Y. Bazilevs, T. Hughes, Weak imposition of Dirichlet boundary conditions in fluid mechanics, Computers & Fluids 36 (2007) 12–26.
[15] Y. Bazilevs, C. Michler, V. Calo, T. Hughes, Weak Dirichlet boundary conditions for wall-bounded turbulent flows, Comput. Methods Appl. Mech. Engrg. 196 (2007) 4853–4862.
[16] W. Wall, M. Frenzel, C. Cyron, Isogeometric structural shape optimization, Comput. Methods Appl. Mech. Engrg. 197 (2008) 2976–2988.
[17] T. Hughes, A. Reali, G. Sangalli, Efficient quadrature for NURBS-based isogeometric analysis, Comput. Methods Appl. Mech. Engrg. 199 (2010) 301–313.
[18] D. Chapelle, K. Bathe, The inf-sup test, Computers & Structures 47 (1993) 537–545.
[19] K. Bathe, The inf-sup condition and its evaluation for mixed finite element methods, Computers & Structures 79 (2001) 243–252.
[20] U. Ghia, K. Ghia, C. Shin, High-Re Solution for Incompressible Flow Using the Navier-Stokes Equations and a Multigrid Method, Journal of Computational Physics 48 (1982) 387–411.
[21] E. Erturk, T. Corke, C. Gokcol, Numerical solutions of 2-d steady incompressible driven cavity flow at high Reynolds numbers, Int. J. Numer. Meth. Fluids **48** (2005) 747–774.
[22] L. Lee, A class of high-resolution algorithms for incompressible flows, Computers & Fluids 39 (2010) 1022–1032.

Wall-Driven Annular Cavity									
Degree	$q = r = 2$								
Knots	$\Xi = \Phi = \{0, 0, 0, 1, 1, 1\}$								
Point	1	2	3	4	5	6	7	8	9
$\bar{x}_1$	0	1	1	0	3/2	3/2	0	2	2
$\bar{x}_2$	1	1	0	3/2	3/2	0	2	2	0
w	1	$1/\sqrt{2}$	1	1	$1/\sqrt{2}$	1	1	$1/\sqrt{2}$	1

Forced Elliptic Cavity									
Degree	$q = r = 2$								
Knots	$\Xi = \Phi = \{0, 0, 0, 1, 1, 1\}$								
Point	1	2	3	4	5	6	7	8	9
$\bar{x}_1$	$-2/\sqrt{2}$	0	$2/\sqrt{2}$	$-4/\sqrt{2}$	0	$4/\sqrt{2}$	$-2/\sqrt{2}$	0	$2/\sqrt{2}$
$\bar{x}_2$	$-1/\sqrt{2}$	$-2/\sqrt{2}$	$-1/\sqrt{2}$	0	0	0	$1/\sqrt{2}$	$2/\sqrt{2}$	$1/\sqrt{2}$
w	1	$1/\sqrt{2}$	1	1	$1/\sqrt{2}$	1	1	$1/\sqrt{2}$	1

Lid-Driven Square Cavity									
Degree	$q = r = 1$								
Knots	$\Xi = \Phi = \{0, 0, 1/2, 1, 1\}$								
Point	1	2	3	4	5	6	7	8	9
$\bar{x}_1$	0	1/2	1	0	1/2	1	0	1/2	1
$\bar{x}_2$	0	0	0	1/2	1/2	1/2	1	1	1
w	1	1/2	1	1/2	1/4	1/2	1	1/2	1

Table A.2: Polynomial degrees, knot vectors, control points and weights for the geometry of the analysed problems.